Probing the ^{12}C+^{12}C fusion reaction via zero-degree spectator measurement in the ^{12}C(^{14}N,αd)^{20}Ne quasi-free reaction*

Xue-Jian Wang (王雪建)[1] Qun-Gang Wen (文群刚)[1†] Cheng-Bo Li (李成波)[2‡] Hui-Ming Jia (贾会明)[3§] Jian-You Guo (郭建友)[1¶] Cheng-jian Lin (林承键)[3] Lei Yang (杨磊)[3] Feng Yang (杨峰)[3] Nan-ru Ma (马南茹)[3] Pei-wei Wen (温培威)[3] Tian-peng Luo (骆天鹏)[3] Chang Chang (常昶)[3] Xue-peng Sun (孙学鹏)[3] Hai-rui Duan (段海锐)[3] Zhi-jie Huang (黄志杰)[3] Cheng Yin (尹诚)[3] Jiong-he Yang (杨炅和)[3]

[1]School of Physics, Anhui University, Hefei 230601,China
[2]Institute of Radiation Technology, Beijing Academy of Science and Technology, Beijing 100089, China
[3]Department of Nuclear Physics, China Institute of Atomic Energy, Beijing 102413, China

Abstract: The ^{12}C+^{12}C fusion reaction is a key physical process in stellar evolution and supernova explosions. It determines the late evolutionary fate of massive stars and directly influences the critical conditions for triggering Type Ia supernovae in accreting white dwarfs. In this work, the Trojan horse method (THM) was employed to investigate the ^{12}C(^{12}C,α_0)^{20}Ne reaction channel of the ^{12}C+^{12}C fusion process, using ^{14}N as the Trojan horse nucleus. Detector telescopes were placed at 0° and 15° to establish two experimental configurations covering the forward-angle regions where spectator particles are most likely to emerge. By applying the distorted-wave Born approximation (DWBA), two sets of astrophysical $S^*(E)$ factors for the two-body reaction ^{12}C(^{12}C,α_0)^{20}Ne were extracted from the three-body reaction ^{12}C(^{14}N,αd)^{20}Ne and normalized to existing experimental data. The results show that, owing to the overall experimental resolution, the present study cannot resolve fine resonance structures. Within the astrophysical energy region of 0.5−2 MeV, the extracted $S^*(E)$ factor exhibits an increasing trend toward lower energies. The $S^*(E)$ factor obtained with the 0° configuration shows a flatter trend than that obtained with the 15° configuration. On the basis of the quasi-free reaction simulation results, the divergence between the two data sets may reflect a combination of experimental acceptance effects, finite detector resolution, and possible differences in the relative contributions of reaction mechanisms. This study provides a systematic examination of the experimental design, quasi-free event selection strategy, and interpretation of the underlying physical mechanisms, serving as a useful reference for understanding the role of the ^{12}C+^{12}C fusion reaction in astrophysical processes.

Keywords: ^{12}C+^{12}C fusion, *S*(E)* factor, Trojan horse method, quasi-free

DOI: 10.1088/1674-1137/aeb3f8 **CSTR:**

CPC Accepted

I. INTRODUCTION

Nuclear reactions in astrophysical environments are fundamental to the synthesis of elements in nature and play a pivotal role in elucidating the origin and evolution of the universe [1−3]. In stellar interiors, nuclear reactions occur predominantly within the Gamow window, where the thermal motion of charged particles provides sufficient energy to overcome the Coulomb barrier. Carbon burning is one of the key processes in the late stages of stellar evolution, typically after the main-sequence phase. It plays a particularly important role in massive stars [4−6]. This process not only dictates the evolutionary pathways of massive stars but also determines the critical ignition conditions for Type Ia supernovae in accreting white dwarf systems.

The typical temperature for carbon burning in stellar environments is about 0.8 GK, corresponding to a center-of-mass energy of $E_G \approx 1.5 \pm 0.3$ MeV. More generally, the temperature range of $0.6-1.2$ GK corresponds to center-of-mass energies of roughly $1-3$ MeV in nuclear astrophysics studies. The carbon-burning reaction in stars proceeds mainly through the following decay

Received 22 May 2026; Accepted 13 October 2026

* This work was supported by the National Natural Science Foundation of China (Grant Nos. 12075031, 12275360, 12475115, and 11935001), the Natural Science Foundation of Beijing Municipality (1222022), and the Doctoral Foundation of the Anhui Provincial Department of Education (2025AHGXZK50097).

† E-mail: qungang@ahu.edu.cn
‡ E-mail: lichengbo@bjast.ac.cn
§ E-mail: jiahm@cnncmail.cn
¶ E-mail: jianyou@ahu.edu.cn

©2026 Chinese Physical Society and the Institute of High Energy Physics of the Chinese Academy of Sciences and the Institute of Modern Physics of the Chinese Academy of Sciences and IOP Publishing Ltd. All rights, including for text and data mining, AI training, and similar technologies, are reserved.

channels [7−9]:

$$^{12}\mathrm{C}\left(^{12}\mathrm{C},\alpha\right)^{20}\mathrm{Ne(Q=4.62MeV)}$$
$$^{12}\mathrm{C}\left(^{12}\mathrm{C},\mathrm{p}\right)^{23}\mathrm{Na(Q=2.24MeV)}$$
$$^{12}\mathrm{C}\left(^{12}\mathrm{C},\mathrm{n}\right)^{23}\mathrm{Mg(Q=-2.62MeV)}$$

In the low-energy region dominated by the Coulomb barrier, the ^{12}C+^{12}C fusion reaction has long been a central topic in nuclear astrophysics because of its critical role in stellar evolution and nucleosynthesis [10−12]. As the energy decreases, the reaction cross section drops steeply, and the strong Coulomb barrier makes direct measurements of the ^{12}C+^{12}C cross section within the Gamow window extremely challenging. This difficulty is further compounded by possible low-energy or subthreshold resonances, whose energies and strengths remain uncertain but could significantly enhance the cross section [13−16].

Current direct measurements of the ^{12}C+^{12}C reaction reach down to $E_{\mathrm{cm}} \approx 2.1$ MeV [7, 8, 15, 19]. At lower energies, the astrophysical $S^*(E)$ factor is largely inferred from theoretical extrapolations, which suffer from significant uncertainties due to possible molecular-like resonances [17, 18, 20]. To address these limitations, indirect approaches such as the Trojan Horse Method (THM) have been widely employed to provide complementary access to low-energy reaction dynamics [20−22, 50]. Tumino, Spitaleri *et al.* first applied the THM to investigate the ^{12}C(^{12}C,α)^{20}Ne and ^{12}C(^{12}C,p)^{23}Na reactions in the energy range of 0.8–2.7 MeV [12], using ^{14}N as the Trojan horse nucleus to provide the participant ^{12}C nucleus and the spectator deuteron. Their measurements revealed several pronounced resonances within the astrophysical energy region, consistent with the theoretical predictions of Cooper [13]. These resonances suggest a substantial enhancement of the reaction rate at stellar temperatures.

Subsequently, the theoretical approximations used in the THM analysis of the ^{12}C+^{12}C system, such as the plane-wave impulse approximation (PWIA), have been the subject of further discussion. For instance, Mukhamedzhanov *et al.* proposed a modified evaluation of the extracted $S^*(E)$ factor, suggesting a reduced rise at low energies [14]. Further analyses noted that different theoretical treatments could introduce variations in the reproduction of high-energy direct measurement data and lead to differing predictions for the angular distribution of the spectator particle, particularly regarding the forward-angle emission characteristic of the quasi-free mechanism [22]. These discussions highlight the sensitivity of indirect measurements to theoretical inputs and kinematic constraints, emphasizing the need for further experimental verification.

Tan, Boeltzig *et al.* carried out new measurements of this reaction using the SAND (a silicon detector array) system combined with particle-γ coincidence techniques. The extracted $S^*(E)$ factors in the center-of-mass energy range of 2.6 − 5 MeV show overall good agreement with existing direct measurement data [15, 46]. On the theoretical side, Taniguchi and Kimura employed the Antisymmetrized Molecular Dynamics (AMD) model to systematically investigate possible ^{24}Mg resonances formed in the ^{12}C+^{12}C fusion reaction within the Gamow window. Their calculations predicted several 0^+ and 2^+ resonant levels, with energies close to those observed in Tumino's experiment [17, 18].

Meanwhile, Nan, Wang *et al.* indirectly studied ^{24}Mg resonances relevant to ^{12}C+^{12}C fusion using the thick-target inverse kinematics method with the ^{23}Na + p reaction [19]. Resonance parameters extracted via multichannel R-matrix analysis revealed structures in the astrophysical energy region of 0.5 − 2 MeV, with resonance positions consistent with both Tumino's experimental results and the AMD model predictions.

Although direct measurements at low energies are generally more reliable, the THM remains one of the few effective approaches capable of probing the energy region below 2 MeV and extracting reaction cross sections [22, 53]. The reliability of the extracted results depends on the proper identification of quasi-free events and the suppression of competing reaction mechanisms through combined particle-identification and kinematic constraints. Consequently, independent experimental verification using different experimental conditions and event-selection strategies is important for assessing the robustness of THM results.

In the THM framework, the quasi-free mechanism requires that spectator particles emerge predominantly at small forward angles. Based on this principle, we selected ^{14}N(^{12}C+d) as the Trojan horse nucleus and positioned telescope detectors at 0° and 15° to systematically cover different forward angular regions. Furthermore, to investigate the possible dependence of the extracted observables on different spectator kinematic conditions, the intermediate breakup process $^{12}\mathrm{C} + {}^{14}\mathrm{N} \rightarrow {}^{12}\mathrm{C} + {}^{12}\mathrm{C} + {}^{2}\mathrm{H}$ was introduced as an additional kinematic constraint in the data analysis [24, 25]. This approach has already been successfully applied in previous THM studies of the ^{9}Be(p,α)^{6}Li reaction.

This work investigates the two-body reaction ^{12}C(^{12}C,α)^{20}Ne in the astrophysical energy region via the three-body reaction ^{12}C(^{14}N,αd)^{20}Ne. Using two different experimental configurations, detectors were placed to cover distinct forward angular ranges, and the intermediate breakup process was incorporated into the analysis framework. Through these comparative experimental designs and data analysis strategies, the present study aims to evaluate the influence of spectator kinematic selection on the extracted astrophysical $S^*(E)$ factor, offering essential experimental insights for a deeper under-

CPC Accepted

standing of the behavior of this reaction under astrophysical conditions.

II. TROJAN HORSE METHOD

The THM is an indirect measurement method based on the quasi-free reaction mechanism and has been widely applied to study the energy dependence of the astrophysical *S*(E)* factor for two-body reactions of astrophysical interest [22, 26−30]. This method offers notable advantages for investigating charged-particle reactions in the stellar energy region, as it effectively overcomes the suppression caused by electron screening and the Coulomb barrier in direct measurements. In contrast to direct methods, the THM provides access to extremely low energies in the Coulomb-barrier region, thereby enabling the investigation of resonances and even subthreshold resonances that would otherwise remain inaccessible [33, 34, 48, 49, 54].

As shown in Eqs. (1)-(2), a two-body charged-particle reaction of astrophysical interest can be studied indirectly by employing a suitably chosen three-body reaction as a surrogate to probe its reaction mechanism:

$$A + x \rightarrow C + c \tag{1}$$

$$A + a \rightarrow C + c + b \tag{2}$$

A denotes the incident particle; a = (x + b) denotes the Trojan Horse nucleus; x is the participant in the two-body reaction; b is the spectator particle; and C and c are the final reaction products. Under the quasi-free condition of the three-body reaction and according to the principle of energy conservation, the energy correspondence between the target two-body reaction and the selected three-body reaction can be derived:

$$E_{Ax}^{qf} = E_{Aa}\left(1 - \frac{\mu_{Aa}}{\mu_{Bb}}\frac{\mu_{bx}^2}{m_x^2}\right) - \varepsilon_a \tag{3}$$

In Eq. (3), ε_a is the binding energy of the Trojan nucleus. E_{Ax} is the energy interval centered on E_{Ax}^{qf}: $E_{Ax} = (E_{Ax}^{qf} - E_{cut}, E_{Ax}^{qf} + E_{cut})$. Here, E_{cut} is the energy cutoff determined by the momentum width of the Fermi motion. Consequently, for a given beam energy, the two-body reaction can be investigated over an energy interval around the quasi-free point [35−37, 51].

The theoretical foundation of the THM is rooted in nuclear reaction models based on the post-form distorted-wave Born approximation (DWBA) of the T-matrix element [22, 23]. Under the surface approximation, the cross section of a three-body reaction can be expressed in terms of the S-matrix element of the corresponding two-body reaction. The theoretical framework of the THM was first introduced by Baur *et al.* in 1986 [38]. As shown in Eq. (4), within the quasi-free mechanism of direct reactions and using the plane-wave impulse approximation (PWIA), the three-body cross section can be factorized into three components associated with the two-body reaction: the kinematical factor K_F, the momentum distribution $|W|^2$ of the Trojan horse nucleus, and the two-body cross section under the half-off-energy-shell (HOES) condition:

$$\frac{d^3\sigma}{dE_{Cc}d\Omega_{Bb}d\Omega_{Cc}} = K_F|W|^2\left(\frac{d\sigma}{d\Omega}\right)_{Ax\rightarrow Cc}^{HOES} \tag{4}$$

Typel *et al.* subsequently conducted a systematic and comprehensive study of THM theory [39, 40, 52]. Starting from the exact three-body reaction T-matrix, they applied the DWBA and used the surface approximation to establish a connection between the three-body reaction cross section and the two-body reaction S-matrix. With additional simplifications, such as the local momentum approximation, the three-body reaction cross section can be factorized into three components, in a form analogous to that derived under the PWIA. Within this theoretical framework, the extracted two-body reaction cross section intrinsically includes the Coulomb penetration factor [41−43]:

$$\frac{d^3\sigma}{dE_{Cc}d\Omega_{Bb}d\Omega_{Cc}} = K_F|W|^2\sum_l p_l\left(\frac{d\sigma_l}{d\Omega}\right)_{Ax\rightarrow Cc}^{OES} \tag{5}$$

In Eq. (5), K_F denotes the kinematic factor, and $|W|^2$ represents the momentum distribution of the spectator inside the Trojan Horse nucleus, given by the squared Fourier transform of the intercluster radial wave function. The factor p_l is identified as the Coulomb penetration correction factor for angular momentum l; it is introduced to remove the effect of the Coulomb barrier and thereby recover a smoother intrinsic energy dependence.

In the present analysis, the Coulomb penetration factor p_l was calculated primarily for the $l = 0$ partial wave. We also evaluated the possible contributions from higher partial waves and found their influence on the overall shape of the extracted $S^*(E)$ factor to be negligible compared with the dominant $l = 0$ term. Because the absolute magnitude of the THM $S^*(E)$ factor is normalized to direct experimental data, this approximation does not affect our main conclusions regarding its energy dependence [31, 32].

As illustrated in Fig. 1, this experiment employs ^{14}N as the Trojan horse nucleus. In the phenomenological THM treatment, the ^{14}N nucleus is approximated by a dominant ^{12}C+d cluster configuration. By selecting appropriate kinematic conditions, the momentum transfer to

CPC Accepted

the d nucleus during the reaction can be minimized and made negligible compared with that to ^{12}C. Under these conditions, the nuclear reaction can be effectively treated as occurring between two ^{12}C nuclei, while the d nucleus acts as a spectator and essentially retains the energy and momentum it possessed inside the parent ^{14}N nucleus. Within this framework, the ^{12}C nucleus is designated as the participant in the quasi-free reaction, the d nucleus as the spectator, and the parent ^{14}N nucleus as the Trojan horse nucleus.

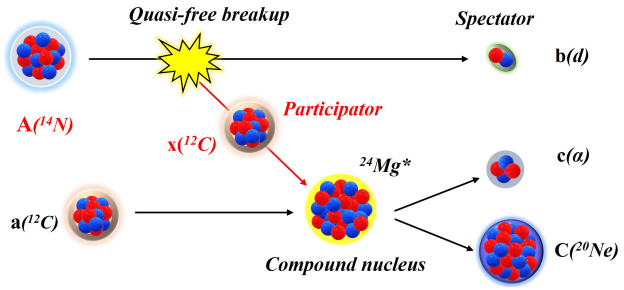

Fig. 1. (color online) Schematic diagram of the Trojan horse method. In the present study, A = (x + b) denotes the incident particle, i.e., the Trojan Horse nucleus, where x is the participant in the two-body reaction and b is the spectator; C and c denote the final products.

III. EXPERIMENT

The THM requires kinematically complete measurement of the three-body reaction $^{12}C + {}^{14}N \rightarrow \alpha + {}^{20}Ne + d$. According to the conservation of energy and momentum, at least two of the three outgoing particles must be detected. In this work, the charged α particles and deuterons were selected to obtain complete kinematic information on the quasi-free process. To measure the energies and emission angles of the outgoing particles precisely, a $\Delta E - E$ silicon telescope detection system was employed. Each telescope consisted of a 20 μm single-sided silicon detector (SSSD) and position-sensitive detectors (PSDs) with thicknesses of 500 μm and 1000 μm. This setup enabled particle identification and energy determination, allowing accurate extraction of the α-particle and deuteron information.

As shown in Figs. 2 and 3, two experimental layouts were designed for this study. In the configuration shown in Fig. 2, the telescope detectors were placed at ±15° and ±45°, covering angular ranges of ±(7°~23°) and ±(35°~55°), respectively, to detect α-d coincidence events. This setup is comparable to that employed by Tumino *et al.* [12]. In the configuration shown in Fig. 3, the detectors were positioned at 0°, ±30°, and -60°, covering angular ranges of -8°~8°, ±(18°~42°), and -48°~-72°, respectively, to facilitate measurements of spectator particles near zero degrees. Among these detectors, those located at ±15° in Fig. 2 and at 0° in Fig. 3 were specifically dedicated to measuring the spectator deuteron.

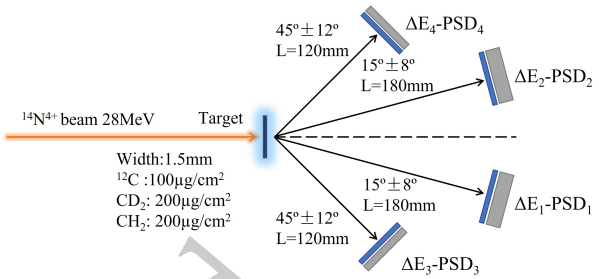

Fig. 2. (color online) Layout and schematic diagram of the detector setup (Configuration 1). The detectors were positioned at ±15° and ±45°, covering angular ranges of ±(7°~23°) and ±(35°~55°), respectively, to detect α–d coincidence events. This setup is comparable to that used by Tumino *et al.* (2018) [12].

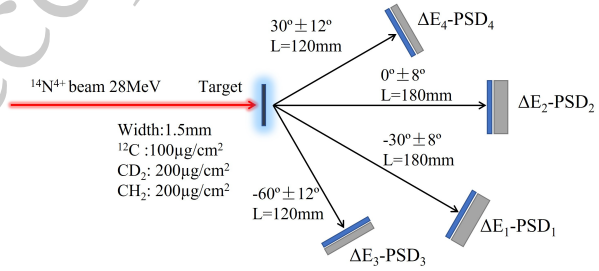

Fig. 3. (color online) Layout and schematic diagram of the detector setup (Configuration 2). The detectors were positioned at 0°, ±30°, and -60°, covering angular ranges of -8°~8°, ±(18°~42°), and -48°~-72°, respectively, to facilitate measurements of the spectator near zero degrees.

This angular configuration was designed to maximize the detection efficiency for quasi-free reaction events. The detector configurations were as follows: Detector 1: 30 μm Al + 20 μm SSSD + 1000 μm PSD; Detector 2: 15 μm Cu + 20 μm SSSD + 1000 μm PSD; Detector 3: 20 μm SSSD + 500 μm PSD; Detector 4: 20 μm SSSD + 500 μm PSD.

Because the quasi-free reaction mechanism requires spectator deuterons to be concentrated in the forward small-angle region, where detectors are particularly susceptible to background interference from the incident beam, beam-stopper foils were installed in front of Detectors 1 and 2. Specifically, copper and aluminum foils with thicknesses of 15 μm and 30 μm, respectively, were used to suppress background contributions from the beam, particularly those from heavy ions such as C and N. These foils still allow light charged particles, including protons, deuterons, and alpha particles, to pass through.

The signals recorded by the PSDs were directly correlated with particle energies and emission angles. The PSDs achieved a position resolution of approximately 0.3

CPC Accepted

mm and an energy resolution of ~45 keV for a 5.5 MeV α source. To ensure measurement accuracy, spatial calibration of the PSDs was performed using an evenly spaced calibration mask, while energy calibration was conducted using a standard α radioactive source together with the elastic scattering reactions ^{14}N(p, p)^{14}N and ^{14}N(d, d)^{14}N.

The experiment was conducted at the HI-13 tandem accelerator facility of the China Institute of Atomic Energy (CIAE), Beijing. According to Eq. (3), a beam energy of 28 MeV for $^{14}N^{4+}$ was selected, corresponding to a quasi-free energy of $E_{Ax}^{qf} = 1.5$ MeV, to effectively cover the Gamow window of $E_{\rm c.m.} = 1-2$ MeV. The beam, with currents ranging from 10 to 40 nA, bombarded a ^{12}C target with a thickness of 100 μg/cm^2 and a width of 1.5 mm.

IV. DATA ANALYSIS

A. Q-value of the three-body reaction ^{12}C(^{14}N,αd)^{20}Ne

Fig. 4 presents the $\Delta E - E$ spectrum, in which the vertical axis corresponds to the energy deposited in the first-layer SSSD and the horizontal axis corresponds to the energy deposited in the second-layer PSD. Owing to their distinct energy-loss characteristics, well-defined particle bands appear in the two-dimensional plot. The red arrow marks the alpha-particle band in the upper-right region, which is well separated from the light ions. The yellow arrow indicates the lower-left region, where $Z = 1$ light charged particles (protons and deuterons) are concentrated.

Although the proton and deuteron loci partially overlap in the low-energy region, event identification does not rely solely on graphical $\Delta E - E$ gating. Candidate $Z = 1$ events are further subjected to multitiered kinematic constraints, including strict three-body Q-value reconstruction and intermediate-breakup selection. Protons originating from competing channels, such as ^{12}C(^{14}N,αp)^{21}Ne, induce a substantial kinematic shift if misidentified as deuterons, causing their reconstructed Q-values to fall well outside the target α_0 window. Consequently, potential proton contamination is effectively suppressed, minimizing its impact on the target ^{12}C(^{14}N,αd)^{20}Ne events.

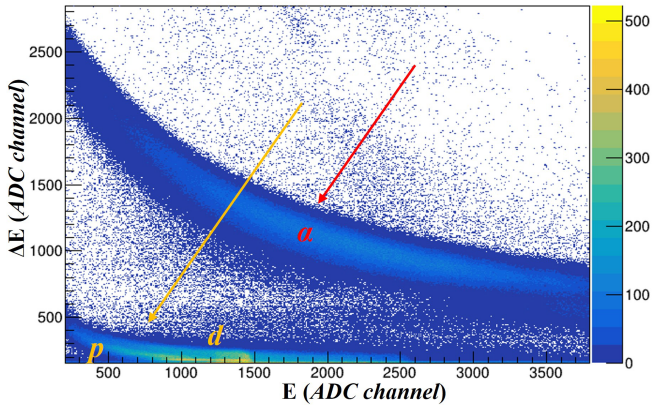

Fig. 4. (color online) A typical $\Delta E - E$ spectrum. The distinct energy-loss characteristics of different particles give rise to well-defined energy bands in the two-dimensional $\Delta E - E$ plot.

The spatial calibration of the position-sensitive detectors was performed using a uniformly spaced calibration grating, and the energy response was calibrated using a standard α radioactive source together with the elastic scattering reactions ^{14}N(p, p)^{14}N and ^{14}N(d, d)^{14}N. Figure 5 shows the PSD energy-position calibration, in which the horizontal axis represents the detector angle and the vertical axis represents the deposited particle energy. The red curve corresponds to the theoretical energy distribution of protons from ^{14}N(p, p)^{14}N elastic scattering, whereas the bright yellow regions represent the energy deposition of scattered protons recorded by the PSD. As shown, the experimental data agree closely with the theoretical curve, confirming the reliability of both the energy and spatial calibrations and providing a robust basis for subsequent quantitative analyses.

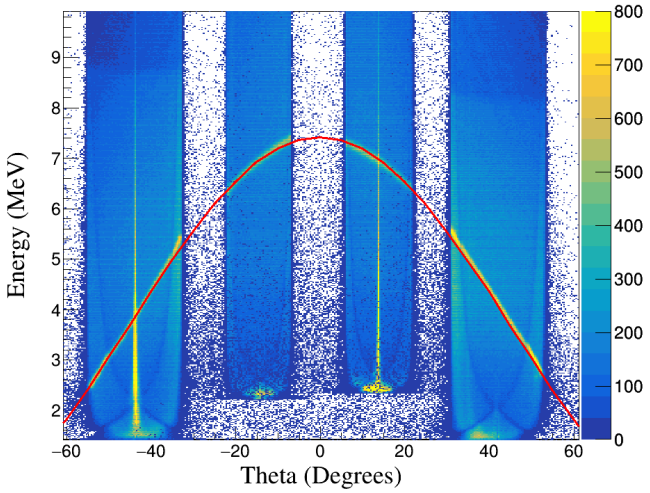

Fig. 5. (color online) Energy and position calibration of the PSD. The red curve shows the theoretical energy distribution of protons from ^{14}N(p, p)^{14}N elastic scattering, whereas the yellow points represent the measured energy deposited by the scattered protons.

The reaction Q value is a fundamental observable that characterizes the energy balance of a nuclear reaction. Fig. 6 shows the reconstructed three-body Q-value spectrum for the ^{12}C(^{14}N,αd)^{20}Ne reaction. The fitted centroid positions of the two dominant peaks, located at −5.65 MeV and −7.28 MeV, are consistent with the theoretical Q values for transitions to the ground state (α_0) and first excited state (α_1) of the residual nucleus, respectively. In addition, the structures observed between approximately

CPC Accepted

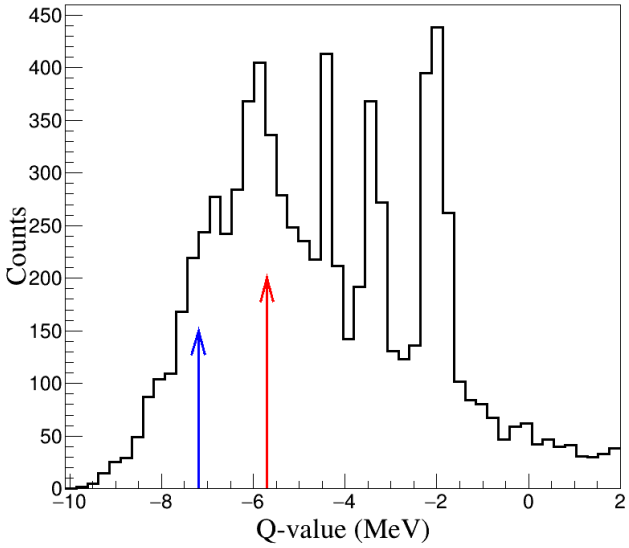

Fig. 6. (color online) Q-value spectrum for the ^{12}C(^{14}N,αd)^{20}Ne reaction. The intersections of the red and blue solid lines with the Q-value axis at -5.65 and -7.28 MeV correspond to contributions from the ground state and the first excited state of the residual nucleus, respectively.

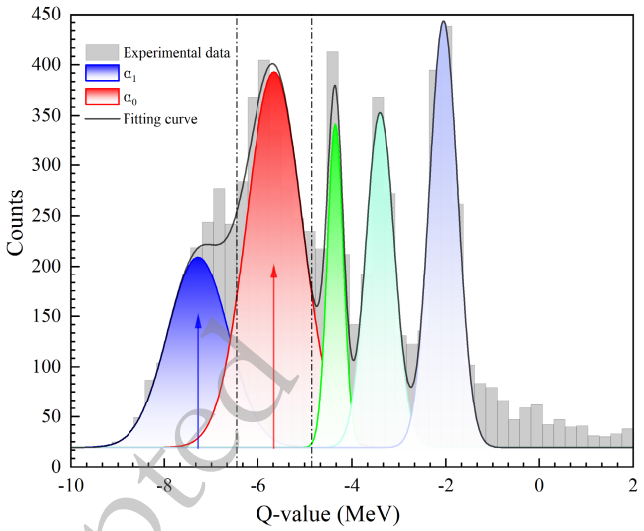

Fig. 7. (color online) Gaussian fit to the Q-value spectrum for the ^{12}C(^{14}N,αd)^{20}Ne reaction. The green shaded area represents background events, whereas the red and blue shaded areas correspond to the ground state and first excited state, respectively.

−1 MeV and −5 MeV mainly originate from competing reaction channels, such as the ^{12}C(^{14}N,αp)^{21}Ne reaction and its excited states, reconstructed under the $\alpha + d$+^{20}Ne hypothesis.

As shown in Fig. 7, the experimental Q-value spectrum is described by a multi-Gaussian fit, in which the green component represents the background contribution, whereas the red and blue components correspond to the α_0 and α_1 transitions, respectively. The multi-Gaussian function used in the fit is expressed as follows:

$$y = y_0 + \frac{A}{w\sqrt{\pi/2}} \exp\left[-2\left(\frac{x - x_c}{w}\right)^2\right] \tag{6}$$

In Eq. (6), y_0 is the baseline offset, A is the total area under the peak, x_c is the peak centroid position, and w denotes the width parameter. The fit reproduces the experimental spectrum well, yielding a coefficient of determination of $R^2 = 0.94$. The fitted width parameters for the α_0 and α_1 peaks are $w_{\alpha_0} = 1.20 \pm 0.10$ MeV and $w_{\alpha_1} = 1.29 \pm 0.15$ MeV, corresponding to standard deviations of $\sigma_{\alpha_0} = 0.60 \pm 0.05$ MeV and $\sigma_{\alpha_1} = 0.64 \pm 0.08$ MeV, respectively. The derived full widths at half maximum (FWHM) are $\mathrm{FWHM}_{\alpha_0} = 1.41 \pm 0.12$ MeV and $\mathrm{FWHM}_{\alpha_1} = 1.52 \pm 0.18$ MeV, which are consistent with each other within experimental uncertainties. Owing to the finite experimental energy resolution, the broad α_0 and α_1 peaks overlap substantially. In the overlap region, the combined statistical contributions of both peaks increase the experimental counts, leading to an apparent shift in peak position and a distortion of the spectral shape. The FWHM value of approximately 1.4 – 1.5 MeV extracted from the fit reflects the total width of the reconstructed three-body Q-value spectrum rather than the intrinsic energy resolution of the detector system.

$$P(A|B) = \frac{P(AB)}{P(B)} = \frac{P(B|A) \cdot P(A)}{P(B)} \tag{7}$$

To focus on the α_0 channel, the present analysis adopts a Q-value gate of -5.65 ± 0.8 MeV, which reduces the influence of competing reaction channels while maintaining sufficient count statistics. To quantitatively evaluate peak overlap and background effects within this candidate region, the Bayesian method introduced in Eq. (7) is used to estimate the statistical contributions of overlapping α_1 events and other competing processes. The resulting contamination is estimated to be less than 10%, thereby minimizing the influence of background events.

It should be emphasized that identification of the α_0 channel is not based solely on the Bayesian analysis. Instead, the final event selection is achieved by combining multiple selection criteria, including particle identification, detector-geometry constraints, reconstructed three-body Q values, and the quasi-free kinematic conditions described by Eqs. (8)–(10). This approach effectively suppresses contributions from competing reaction channels.

B. Selection of Quasi-Free Reaction Events

Fig. 8 illustrates a possible intermediate breakup process of the Trojan horse nucleus during the reaction, specifically ^{12}C + ^{14}N → ^{12}C + ^{12}C + ^{2}H. By combining the physical quantities shown in Fig. 8 with the principles of

CPC Accepted

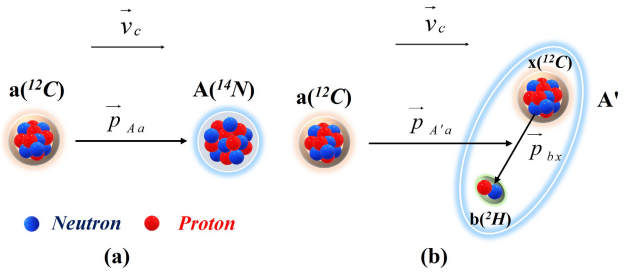

Fig. 8. (color online) Schematic illustration of the intermediate breakup process ^{12}C + ^{14}N → ^{12}C + ^{12}C + ^{2}H. Here, $\vec{v}_c$ denotes the velocity in the center-of-mass frame.

energy and momentum conservation, Eqs. (8)-(10) can be derived [24, 25].

$$\frac{p_{A'a}^2}{2\mu_{A'a}} + \frac{p_{bx}^2}{2\mu_{bx}} = \frac{p_{Aa}^2}{2\mu_{Aa}} + Q' \tag{8}$$

$$Q' = (m_A - m_b - m_x)c^2 \tag{9}$$

$$\overrightarrow{p_{bx}} + \frac{m_b}{m_{A'}}\overrightarrow{p_{A'a}} + m_b\overrightarrow{v_c} = \overrightarrow{p_b} \tag{10}$$

In Eq. (10), $\overrightarrow{p_b}$ denotes the momentum of particle b (^{2}H) in the laboratory frame, whereas particle a (^{12}C) is the stationary target nucleus in the experiment. Using Eqs. (8)-(10), the momentum of particle b (^{2}H), obtained from the experimental data, can be used to calculate either $p_{A'a}$ or p_{bx}. A positive real value of the calculated $p_{A'a}$ or p_{bx} indicates the occurrence of the intermediate breakup process ^{12}C + ^{14}N → ^{12}C + ^{12}C + ^{2}H. This condition was adopted as one of the criteria for selecting quasi-free events.

In applications of the THM, quasi-free events are typically selected by imposing constraints on the spectator momentum. However, in the study of the ^{9}Be(p,α)^{6}Li reaction [22, 23], restricting only the spectator momentum was found to be insufficient for effectively excluding contributions from cascade processes, which can enhance resonance structures. To address this issue, subsequent analyses incorporated the intermediate breakup process on the basis of energy- and momentum-conservation relations, thereby imposing both kinematic and dynamical constraints on quasi-free events.

This approach improved the physical reliability of event selection and yielded reliable bare-nucleus cross-section data. Therefore, we introduce the intermediate breakup process as an additional selection condition to further strengthen the physical constraints on event selection and enhance the reliability of quasi-free event identification.

Fig. 9 presents the relative energy spectra of ^{20}Ne and α particles before and after application of the intermediate breakup (BU) kinematic constraints. It is important to emphasize the sequence of the event selection procedure: before these relative energy spectra were constructed, a Q-value gate of -5.65 ± 0.8 MeV had already been imposed on all candidate events. Consequently, the prominent background structures observed at higher Q values in Fig. 7 (e.g., around -2, -3.5, and -4.4 MeV, which originate from competing channels such as $p+\alpha+^{21}$Ne) were suppressed to the greatest extent possible before the analysis shown in Fig. 9.

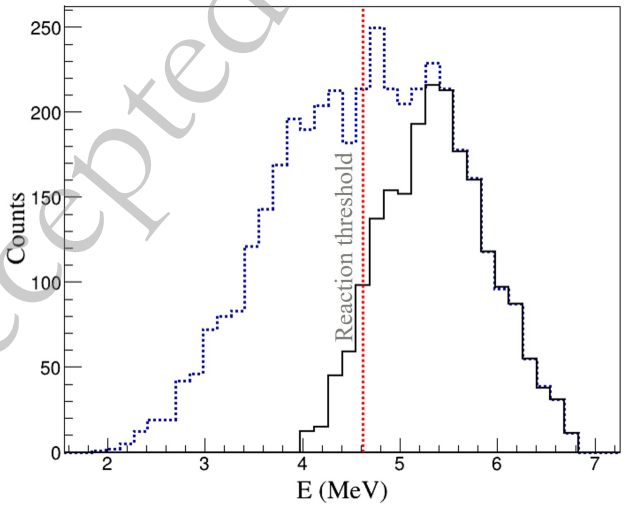

Fig. 9. (color online) Relative energy spectra of the ^{20}Ne–α system with the intermediate-breakup-process constraint applied. The blue dashed and black solid histograms represent the spectra before and after applying the constraint, respectively.

In Fig. 9, the blue dashed and black solid histograms represent the Q-gated spectra before and after application of the intermediate breakup constraints, respectively, and the red dashed line marks the reaction threshold at 4.62 MeV. As clearly shown in the figure, imposing the intermediate breakup condition further suppresses residual background events near the reaction threshold, thereby reducing background contamination for the target ^{12}C(^{12}C,α_0)^{20}Ne channel.

C. Analysis of the Deuteron Momentum Distribution

The momentum distribution of the spectator deuteron is a highly sensitive observable for investigating the reaction mechanism because it provides a direct means of validating the selection of quasi-free events. According to the quasi-free reaction mechanism, the momentum distribution of the spectator particle is expected to reproduce its internal momentum distribution within the parent nucleus.

For the extraction of the astrophysical $S^*(E)$ factor in the center-of-mass energy range of 0.5–2.0 MeV, the spectator-deuteron momentum distribution was recon-

CPC Accepted

structed to examine the quasi-free reaction mechanism. A relatively narrow ^{20}Ne–α relative-energy window of 50–100 keV was adopted so that the quantity $p_l \frac{d\sigma_l}{d\Omega}$ could be regarded as approximately constant within each energy interval. The center of the selected energy window was varied across the investigated energy range to maintain sufficient statistics while minimizing the influence of energy broadening. In addition, the event sample was further constrained by the intermediate-breakup selection and the kinematic conditions described by Eqs. (8)–(10).

The momentum distribution of the spectator deuteron serves as an important criterion for verifying the validity of the quasi-free reaction mechanism. Therefore, the experimentally reconstructed momentum distribution was compared with theoretical calculations. Preliminary candidate events for the reaction channel of interest were selected using $\Delta E - E$ particle identification, experimental geometrical constraints, and three-body kinematic Q-value reconstruction. Kinematic constraints from the intermediate breakup process were then applied to further suppress contributions from competing reaction mechanisms. On this basis, the agreement between the experimental spectator-deuteron momentum distribution and the theoretical quasi-free distribution was analyzed to determine the optimal quasi-free event-selection region for subsequent analysis.

In Fig. 10, the reconstructed spectator-deuteron momentum distribution for the ^{12}C(^{14}N,αd)^{20}Ne reaction is presented as red solid circles with a momentum-bin width of 10 MeV/c. The error bars represent statistical uncertainties. The black dashed curve shows the theoretical momentum distribution calculated using a Woods–Saxon potential with standard geometrical parameters. The potential depth was slightly adjusted to reproduce the experimental ground-state binding energy of 10.27 MeV for the ^{12}C–d cluster configuration in ^{14}N. The experimental and theoretical distributions were normalized to the same integral for comparison.

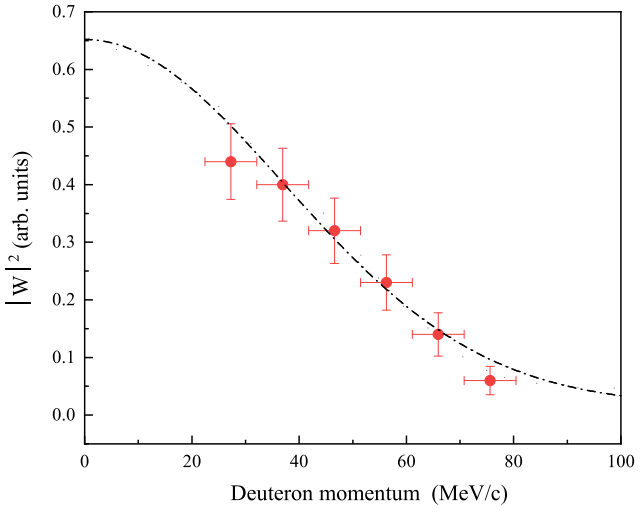

Fig. 10. (color online) Comparison of the experimental momentum distribution of the spectator deuteron (red circles) with the theoretical distribution (black dashed line). Error bars indicate statistical uncertainties.

The absence of experimental data points below approximately 30 MeV/c is mainly associated with the experimental detection threshold. Low-momentum spectator deuterons undergo significant energy losses when passing through the blocking foil and the dead layers of the position-sensitive detector, resulting in reduced detection efficiency in this momentum region. In addition, electronic-noise suppression and event-quality requirements applied during data analysis further reduce the available statistics at low momenta. Therefore, the present momentum distribution is limited to the experimentally accessible region.

For the two experimental setups, the reconstructed spectator-deuteron momentum distribution exhibits a trend consistent with the theoretical quasi-free distribution in the dominant region of 30–80 MeV/c, supporting the adopted spectator-momentum selection. Consequently, the momentum window of $30 < p_d < 80$ MeV/c was adopted for selecting quasi-free events, and the events within this window were used for the subsequent $S^*(E)$ factor analysis.

V. EXTRACTION AND ANALYSIS OF THE ASTROPHYSICAL $S^*(E)$ FACTOR

A. The Astrophysical *S*(E)* Factor

Fig. 11 presents the reconstructed relative-energy (^{20}Ne + α) spectra obtained after applying the complete event-selection chain, which incorporates particle identification, detector-geometry constraints, three-body Q-value gating, intermediate-breakup constraints, and the spectator-momentum cut ($30 < p < 80$ MeV/c). Panels (a) and (b) show the data measured with spectator-deuteron detection centered at 15° and 0°, respectively. Because of the limited experimental energy resolution, possible narrow resonances are broadened during reconstruction and overlap with adjacent structures, producing a broad distribution together with potential non-resonant continuum contributions. Known resonance positions are indicated by vertical arrows as spectroscopic reference points. Rather than imposing an unconstrained multi-component decomposition into individual resonances, which would introduce substantial parameter ambiguities, the present analysis focuses on extracting the robust overall energy dependence of the astrophysical $S^*(E)$ factor across the Gamow window.

In the center-of-mass system, the astrophysical $S^*(E)$ factor of the ^{12}C+^{12}C fusion reaction is defined by Eq. (11):

CPC Accepted

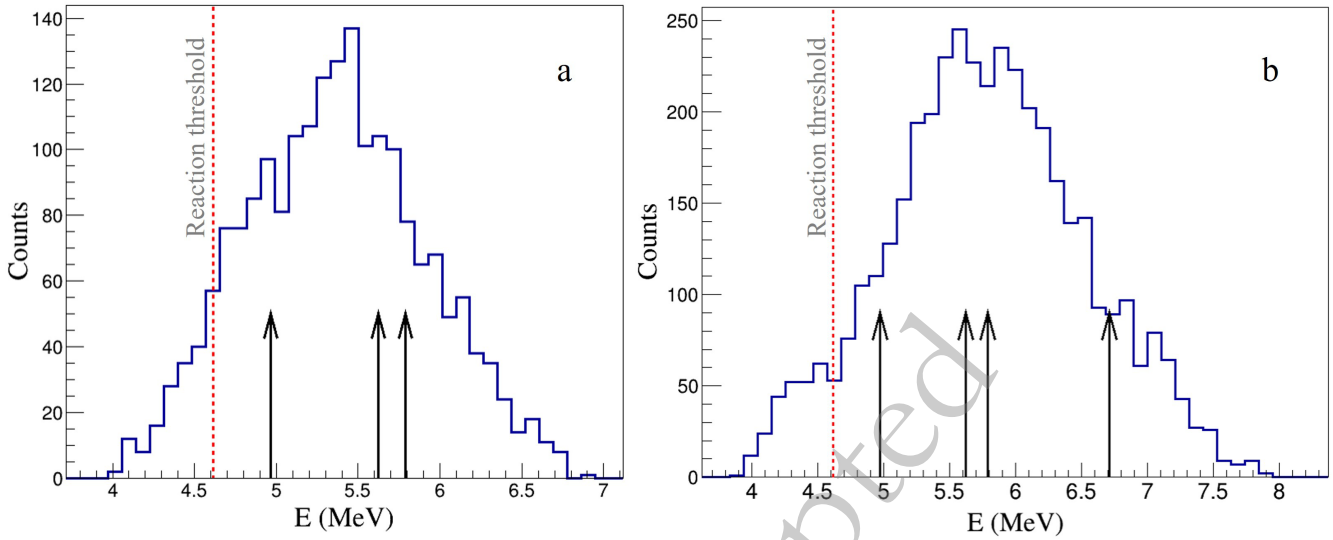

Fig. 11. (color online) Relative energy spectrum for ^{20}Ne and the α particle. (a) Spectator deuteron at a central angle of 15°; (b) spectator deuteron at a central angle of 0°. Resonance structures at 4.967, 5.621, 5.788, and 6.706 MeV are indicated by arrows. These structures correspond to known ^{12}C+^{12}C resonances in the center-of-mass energy range $E_{\rm c.m.}$ = 0–3 MeV.

$$S*(E) = \sigma(E)E\exp\left(\frac{87.21}{\sqrt{E}} + 0.46E\right) \quad (11)$$

By combining multiple selection criteria, including particle identification, angular constraints imposed by the experimental setup, kinematic conditions associated with the intermediate breakup mechanism, and additional Q-value gating, the contributions of competing reaction channels and background events are significantly reduced. Because of the effects of nucleon–nucleon and Coulomb interactions, the present analysis is performed within the framework of the DWBA.

The astrophysical *S*(E)* factor was calculated using Eqs. (5) and (11). The experimentally extracted *S*(E)* factors were then normalized to existing measurements and systematically compared with other experimental data and theoretical model calculations [2, 4, 12, 13, 17, 44]. Fig. 12 shows two sets of *S*(E)* factors for the ^{12}C(^{12}C,α_0)^{20}Ne reaction obtained after quasi-free event selection, represented by black and red solid circles, respectively.

Both data sets were normalized to the data of Tumino et al. [12] and the energy-corrected data of Mazarakis et al. [44], which include the standard +100 keV energy-shift correction recommended by Barnes et al. [47]. The error bars indicate statistical uncertainties. The black solid circles correspond to spectator deuteron angles from 7° to 23°, which is comparable to the experimental condition in Tumino et al. [12], whereas the red solid circles correspond to the range from -8° to 8°.

As shown in Fig. 12, the extracted $S^*(E)$ factors from both data sets are presented. The present $S^*(E)$ factor data indicate that the overall behavior of the ^{12}C+^{12}C reaction in the low-energy region can be viewed as a series

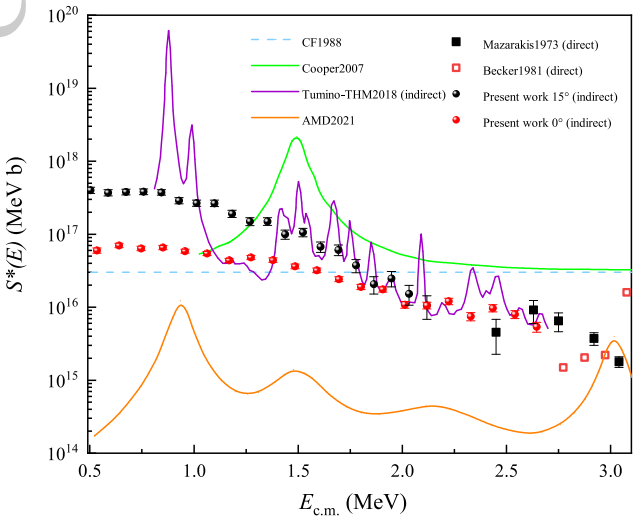

Fig. 12. (color online) Experimentally extracted *S*(E)* factor for the two-body reaction ^{12}C(^{12}C,α_0)^{20}Ne after applying the quasi-free event selection, compared with previously published experimental data and theoretical predictions. Some referenced data sets do not explicitly isolate the α_0 branch but instead include contributions from the inclusive α channel; these data are retained to facilitate comparison of the overall energy dependence. The reference data are taken from Refs. [2, 4, 12, 13, 17, 44]. The error bars indicate statistical uncertainties. The uncertainty in the center-of-mass energy is approximately $\sigma_{E_{\rm c.m.}}$ = 0.3 MeV (FWHM = 0.70 MeV).

of resonance structures superimposed on a relatively flat nonresonant continuum. As the energy decreases, the cumulative superposition of these low-energy resonances drives the overall $S^*(E)$ factor to exhibit an increasing trend from the high-energy to the low-energy region. Without resolving the fine resonance structures, potential

CPC Accepted

narrow resonances may be broadened in energy and overlap with one another. In contrast, the red data points display a flatter energy dependence and remain lower than the black data points in the low-energy region. In addition, the present experimental data show possible bump-like structures around 0.8 and 1.5 MeV, which may be associated with the superposition of broadened resonance contributions.

The uncertainty in the center-of-mass energy is approximately $\sigma_{E_{\mathrm{c.m.}}} = 0.3$ MeV (FWHM = 0.70 MeV). This uncertainty is mainly determined by energy-resolution broadening and geometrical uncertainties in the detection angles. In particular, the angular uncertainty is constrained by the position resolution of the PSD detector, the beam-spot size, and the distance between the detector sensitive area and the target position, which determine the geometrical solid angle and angular acceptance. It is also affected by the accuracy of the detector angular calibration. The energy uncertainty mainly originates from the intrinsic energy resolutions of the PSD and SSSD detectors, uncertainties in energy calibration, uncertainties in the energy-loss correction for the detector dead layers, and energy straggling of the light particles in the beam-stopper foil, with nonuniformity in the foil thickness being an important contributing factor.

Because ^{20}Ne is not directly detected as the third outgoing particle, its momentum and energy are reconstructed entirely from the three-body kinematics through energy and momentum conservation, based on the measured kinematic information of the two light particles (p and α). Therefore, the energy and angular resolutions of the directly measured light particles are propagated through the differential kinematic relations into the reconstructed energy and angular quantities of ^{20}Ne, thereby collectively contributing to the broadening of the total center-of-mass energy.

The present data do not allow a reliable separation of individual resonance contributions. Consequently, the present analysis focuses on the overall energy dependence rather than the fine structure of individual resonances. Multiple selection criteria, including particle identification, angular constraints, three-body Q-value restrictions, intermediate-breakup channel selection, and spectator-deuteron momentum cuts, were applied to both experimental setups. These criteria effectively reduced the contribution of non-quasi-free events. The discrepancy observed between the two data sets in the low-energy region may originate from a combination of several factors: experimental acceptance effects, finite detector resolution, and potential variations in the relative contributions of different reaction mechanisms.

B. Monte Carlo Simulations and Background Analysis

Fig. 13 compares the simulated event yields for the quasi-free and sequential-decay mechanisms under the two experimental configurations. To evaluate the corresponding detection acceptances, 5×10^6 events were generated for each reaction mechanism and propagated through the experimental geometry. The red and black curves represent the accepted quasi-free events for spectator central angles of 0° and 15°, respectively, whereas the blue and green curves correspond to the accepted sequential-decay events for the two configurations. The simulation indicates that the 0° configuration provides higher acceptance for quasi-free events, while reducing the relative contribution of sequential decay under the same selection criteria.

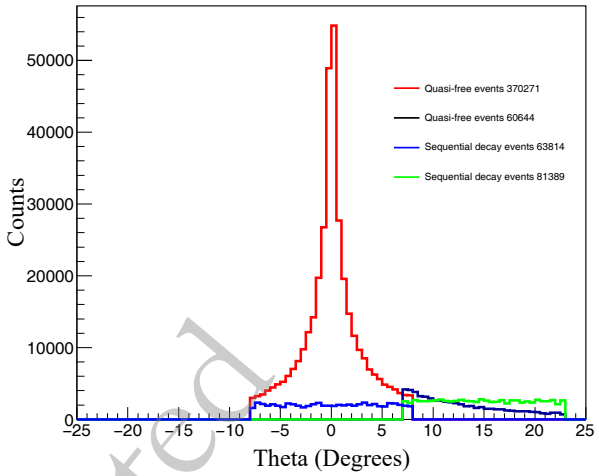

Fig. 13. (color online) Simulated comparison of event counts for quasi-free and sequential decay processes.

Within the THM framework, the quasi-free reaction mechanism is expected to dominate when the spectator particle is emitted close to the beam direction and has low momentum. This expectation is supported by the present Monte Carlo simulations and by the measured spectator angular distribution. Consequently, the 0° configuration is expected to improve the selection efficiency for quasi-free events. If competing reaction mechanisms are not sufficiently suppressed during event selection, their residual contributions may affect the reconstructed observables and consequently influence the extracted astrophysical $S^*(E)$ factor. Therefore, particle identification, three-body Q-value reconstruction, intermediate-breakup selection, and spectator-momentum constraints were applied simultaneously to minimize contributions from competing processes.

C. Discussion of Experimental Results

The differences observed between the results from the two experimental setups can be attributed primarily to the following factors:

(1) The target reaction channel (α_0 channel) is influenced by contributions from the α_1 channel and neighboring reaction channels. Candidate events for the target reaction channel were initially selected using $\Delta E - E$

CPC Accepted

particle identification, experimental geometrical constraints, and three-body kinematic Q-value reconstruction. Subsequently, kinematic constraints from the intermediate breakup process were applied to further suppress contributions from competing reaction mechanisms. Using these criteria, the influence of non-quasi-free events was minimized by reconstructing the spectator-deuteron momentum distribution and comparing it with the theoretical Woods–Saxon distribution.

(2) As shown in Figs. 11(a) and 11(b), a broad structure formed by the superposition of low-energy resonances can still be observed in the center-of-mass energy range of approximately 0–3 MeV. However, the resolution is insufficient to separate adjacent narrow resonances. Fig. 11 demonstrates the presence of resonance contributions in this energy region. Although the $S^*(E)$ factors extracted on this basis exhibit some numerical discrepancies, their overall energy dependences remain consistent.

(3) Monte Carlo simulation results indicate that the two experimental setups differ in their acceptance efficiencies for the quasi-free reaction process. Under the present experimental conditions, the limited statistics, detector resolution, and presence of competing reaction mechanisms prevent the complete elimination of all non-quasi-free contributions. Therefore, the $S^*(E)$ factors extracted in this work are intended primarily to characterize the overall trend in the low-energy region, rather than to provide a precise determination of individual resonance parameters.

In summary, considering the aforementioned experimental constraints and acceptance effects, the primary physical conclusion drawn from the present study is that the low-energy region can be characterized as a series of possible resonance structures superimposed on a relatively flat non-resonant continuum. As the energy decreases, the cumulative superposition of these low-energy resonances leads to an increasing trend in the overall $S^*(E)$ factor.

VI. SUMMARY AND DISCUSSION

In this work, the THM was applied to perform an indirect measurement of the ^{12}C(^{12}C,α_0)^{20}Ne reaction, which plays a crucial role in stellar evolution and supernova explosions. Because direct measurements in the astrophysical energy region are extremely challenging owing to strong Coulomb-barrier suppression, the three-body reaction ^{12}C(^{14}N,αd)^{20}Ne was investigated to extract the astrophysical $S^*(E)$ factor, using ^{14}N as the Trojan horse nucleus.

Based on the quasi-free mechanism, which indicates that spectator particles are emitted primarily in the forward-angle region, the experimental geometry was designed to explore the kinematic phase space in which quasi-free contributions are expected to be significant. The experiment employed a $\Delta E-E$ silicon telescope detection system with two configurations designed to systematically cover distinct forward angular ranges, including measurements near 0°. Furthermore, the intermediate breakup process ^{12}C+^{14}N → ^{12}C+^{12}C+^{2}H was introduced as an additional physical constraint to investigate the influence of spectator kinematic selection.

Based on distorted-wave Born approximation (DWBA) analysis, two sets of astrophysical $S^*(E)$ factors for the ^{12}C(^{12}C,α_0)^{20}Ne reaction were extracted and normalized to the available direct measurements of Mazarakis *et al.* and the previous Trojan Horse Method (THM) results reported by Tumino *et al.* Within the astrophysical energy range of 0.5–2 MeV, the $S^*(E)$ factor exhibits an overall increasing trend with decreasing energy. The results obtained with the 0° configuration display a flatter energy dependence, with generally lower $S^*(E)$ values in the low-energy region. The difference observed between the two data sets in the low-energy region may originate from a combination of several factors: experimental acceptance effects, finite detector resolution, and potential variations in the relative contributions of different reaction mechanisms.

Although the present experiment does not allow a precise determination of individual resonance structures, this comparative study reveals the overall energy dependence of the $S^*(E)$ factor in the 0.5–2.0 MeV region, an issue central to the ongoing debate surrounding the ^{12}C+^{12}C fusion reaction. The present $S^*(E)$ factor data indicate that the overall behavior of the ^{12}C+^{12}C reaction in the low-energy region can be viewed as a series of resonance structures superimposed on a relatively flat non-resonant continuum. As the energy decreases, the cumulative superposition of these low-energy resonances collectively drives the overall $S^*(E)$ factor to exhibit an increasing trend. Moreover, potential narrow resonances may be broadened in energy and overlap with one another, thereby manifesting experimentally as a flatter energy dependence.

Through a systematic examination of the experimental design, quasi-free event selection strategies, and interpretations of the underlying physical mechanisms under two different experimental configurations, these results provide a useful reference for understanding stellar nucleosynthesis and guiding future high-precision measurements. Ultimately, by combining direct measurements, indirect approaches, and theoretical models, the underlying mechanisms of this critical reaction can be further constrained.

Acknowledgments

The authors sincerely thank Prof. Shu-Hua Zhou of the CIAE for his valuable advice and guidance

CPC Accepted

throughout this work. The authors are grateful to the Nuclear Reaction Group at the CIAE for their generous assistance with the experimental preparation and measurements. Special thanks are extended to the staff of the HI-13 tandem accelerator for their strong support in ensuring the successful completion of the experiment.

References

[1] C. A. Bertulani, T. Kajino, Prog. Part. Nucl. Phys. **89**, 56 (2016)
[2] C. E. Rolfs, W. S. Rodney. Cauldrons in the Cosmos: Nuclear Astrophysics. Chicago: University of Chicago Press, 1988.
[3] E. Margaret Burbidge, G. R. Burbidge, William A. Fowler, *et al*., Rev of Mode Phys **29**(4), 547 (1957)
[4] H. W. Becker, K. U. Kettner, C. Rolfs, *et al*., Z. Phys. A **303**, 305 (1981)
[5] T. Spillane, F. Raiola, C. Rolfs, *et al*., Phys. Rev. Lett. **98**, 122501 (2007)
[6] B. Bucher, X. D. Tang, X. Fang, *et al*., Phys. Rev. Lett. **114**, 251102 (2015)
[7] C. L. Jiang, D. Santiago-Gonzalez, S. Almaraz-Calderon, *et al*., Phys. Rev. C **97**, 012801 (2018)
[8] G. Fruet, S. Courtin, M. Heine, *et al*., Phys. Rev. Lett. **124**, 192701 (2020)
[9] L. Morales-Gallegos, M. Aliotta, L. Gialanella, *et al*., Eur. Phys. J. A **60**, 11 (2024)
[10] J. R. Patterson, H. Winkler, C. S. Zaidins., Astrophys. J. **157**, 367 (1969)
[11] N. T. Zhang, X. Y. Wang, D. Tudor, *et al*., Phys. Lett. B **801**, 135170 (2020)
[12] A. Tumino, C. Spitaleri, M. La Cognata, *et al*., Nature **557**, 687 (2018)
[13] R. L. Cooper, A.W. Steiner, E.F. Brown, Astrophys. J **702**, 660 (2009)
[14] A. M. Mukhamedzhanov, D.Y. Pang, A.S. Kadyrov, Phys. Rev. C **99**, 064618 (2019)
[15] W. P. Tan, A. Boeltzig, C. Dulal, *et al*., Phys. Rev. Lett. **124**, 192702 (2020)
[16] T. P. Luo, P. W. Wen, C. J. Lin, *et al*., Chin. Phys. C **46**, 064105 (2022)
[17] Y. Taniguchi, M. Kimura, Phys. Lett. B **823**, 136790 (2021)
[18] Y. Taniguchi, M. Kimura, Phys. Lett. B **849**, 138434 (2024)
[19] W. K. Nan, Y. B. Wang, J Su, *et al*., Phys. Lett. B **862**, 139341 (2025)
[20] X. D. Tang, L. H. Ru, EPJ Web Conf **260**, 10 (2022)
[21] Y. J. Li, X. Fang, B. Bucher, *et al*., Chin. Phys. C **44**, 115001 (2020)
[22] A. Tumino, C. A. Bertulani, S. Cherubini, *et al*., Prog. Part. Nucl. Phys **143**, 104164 (2025)
[23] J. Lei, Phys. Rev. C **111**, 034610 (2025)
[24] Q. G. Wen, C. B. Li, S. H. Zhou, *et al*., Phys. Rev. C **78**, 035805 (2008)
[25] Q. G. Wen, C. B. Li, S. H. Zhou, *et al*., J. Phys. G: Nucl. Part. Phys **38**(8), 085103 (2011)
[26] S. Romano, L. Lamia, C. Spitaleri, *et al*., Eur. Phys. J. A **27**, 221 (2006)
[27] C. Spitaleri, A. M. Mukhamedzhanov, L. D. Blokhintsev, M. L. Cognata, R. G. Pizzone, and A. Tumino, Phys. At. Nucl **74**, 1725 (2011)
[28] M. La Cognata, C. Spitaleri, and A. M. Mukhamedzhanov, Astrophys. J **723**, 1512 (2010)
[29] C. Spitaleri, L. Lamia, A. Tumino, *et al*., Phys. Rev. C **69**, 055806 (2004)
[30] C. B. Li, Q. G. Wen, S. H. Zhou, *et al*., Chin. Phys. C **39**(5), 11 (2015)
[31] C. B. Li, H. M. Jia, Q. G. Wen, *et al*., Phys. Lett. B **879**, 140675 (2026)
[32] C. B. Li, H. M. Jia, Q. G. Wen, *et al*., Phys. Rev. C **114**, 035801 (2026)
[33] M. La Cognata, C. Spitaleri, O. Trippella, *et al*., Phys. Rev. Lett. **109**, 232701 (2012)
[34] X. J. Wang, Q. G. Wen, C. B. Li, *et al*., Phys. Lett. B **854**, 138745 (2024)
[35] C. B. Li, Q. G. Wen, A. Tumino, *et al*., Phys. Rev. C **95**, 035804 (2017)
[36] Q. G. Wen, C. B. Li, S. H. Zhou, *et al*., Phys. Rev. C **93**, 035803 (2016)
[37] C. B. Li and Q. G. Wen, Nucl. Phys. Rev **37**, 626 (2020)
[38] G. BAUR, Phys. Lett. B **178**(2-3), 135 (1986)
[39] C. Spitaleri, S. Typel, R. G. Pizzone, *et al*., Phys. Rev. C **63**, 055801 (2001)
[40] S. Typel and G. Baur, Ann. Phys **305**, 228 (2003)
[41] A. M. Mukhamedzhanov, L. D. Blokhintsev, B. F. Irgaziev, *et al*., J. Phys. G: Nucl. Part. Phys **35**(1), 014016 (2007)
[42] C. Spitaleri, C. A. Bertulani, L. Fortunato, *et al*., Phys. Lett. B **755**, 275 (2016)
[43] C. A. Bertulani, M. S. Hussein, S. Typel, *et al*., Phys. Lett. B **776**, 217 (2018)
[44] M. G. Mazarakis and W. E. Stephens, Phys. Rev. C **7**, 1280 (1973)
[45] C. L. Jiang, K. E. Rehm, B. B. Back and R. V. F. Janssens, Phys. Rev. C **75**, 015803 (2007)
[46] W. P. Tan, A. Gula, K. Lee, *et al*., Phys. Rev. C **110**, 035808 (2024)
[47] C. A. Barnes, S. Trentalange, and S. C. Wu, Treatise on Heavy-Ion Science **6**, 1 (1985)
[48] C. L. Jiang, B. B. Back, H. Esbensen, *et al*., Phys. Rev. Lett. **110**, 072701 (2013)
[49] X. D. Tang, S. B. Ma, X. Fang, *et al*., Nucl. Sci. Tech. **30**, 126 (2019)
[50] A. M. Mukhamedzhanov, D. Y. Pang, C. A. Bertulani, *et al*., Phys. Rev. C **90**, 034604 (2014)
[51] L. Lamia, M. Mazzocco, R.G. Pizzone, *et al*., Astrophys. J **879**(1), 23 (2019)
[52] S. Typel and H. H. Wolter, Few-Body Syst **29**(1-3), 75 (2000)
[53] A. Tumino, C. Spitaleri, Mukhamedzhano. A, *et al*., Phys. Rev. Lett. **98**, 252502 (2007)
[54] X. D. Su, M. La Cognata, N. Vukman, *et al*., Phys. Rev. Lett. **135**, 182701 (2025)

CPC Accepted